4D-MRI for Treatment Planning of Liver Tumors

Jessica Scholey[1]; Horatio Thomas[1]; Xin Miao[2]; Dianne Ferguson[3]; Mary Feng[1]

[1]Department of Radiation Oncology, University of California, San Francisco, CA, USA
[2]Siemens Medical Solutions USA Inc., Boston, MA, USA
[3]Department of Radiation Oncology, Brigham and Women's Hospital, Dana Farber Cancer Institute and
 Harvard Medical School, Boston, MA, USA

Introduction

Stereotactic body radiation therapy (SBRT) is increasingly being used to manage primary and metastatic liver tumors [1–3]. Accurately accounting for respiratory motion is imperative when targeting liver tumors with radiation. Strategies such as abdominal compression and breath-hold have been used to reduce tumor motion, though many patients cannot tolerate these strategies due to coexisting comorbidities and poor performance status. For these patients, four-dimensional computed tomography (4D-CT) is used to estimate tumor motion throughout the respiratory cycle and generate internal target volumes (ITVs) for radiotherapy treatment planning. However, delineating liver tumors on 4D-CT is very challenging because of its inherent poor soft tissue contrast. These tumors can only be visualized using intravenous contrast, which is eliminated from the liver quickly, creating practical challenges in correctly timing contrast administration with image acquisition. Contrast-enhanced 4D magnetic resonance imaging (4D-MRI) offers a promising strategy for directly visualizing liver tumor motion. The superior soft tissue contrast of MRI and long usable duration of hepato-biliary MRI contrast allows the visualization of tumors throughout the respiratory cycle [4,5].

Prior studies have demonstrated 4D-MRI acquisition using multi-slice 2D or 3D sequences with Cartesian or non-Cartesian sampling trajectories [6–10]. Despite increased interest, clinical implementation of 4D-MRI technology has been limited because it requires specialized acquisition protocols, reconstruction techniques, and hardware. In this study, we adopted a novel 4D-MRI technique[1] that performs continuous volumetric scanning with self-gating and retrospective respiratory binning that can capture irregular respiratory motion. We assessed the feasibility of using 4D-MRI in target volume generation for liver tumors and compared 4D-MRI with 4D-CT in terms of liver tumor clarity and the dosimetry of radiation treatment plans [11].

Materials and methods

Image acquisition and reconstruction
Twelve patients undergoing SBRT to the liver were prospectively recruited into this IRB-approved study. All patients received same-day 4D-CT and 4D-MRI simulation using identical positioning and immobilization. 4D-CT scans were acquired over a single respiratory cycle (120 kVp, 0.98 × 0.98 mm voxels, 3 mm slice thickness, scan time ~1 minute) and retrospectively binned using 8-phase reconstruction (SOMATOM Definition AS, Siemens Healthcare, Forchheim, Germany).

MRIs were acquired on a 3 Tesla MRI simulator (MAGNETOM Vida, Siemens Healthcare, Erlangen,

[1]Work in progress. The application is currently under development and is not for sale in the U.S. and in other countries. Its future availability cannot be ensured.

Germany) using a large 18-channel UltraFlex coil suspended from a coil bridge and a 32-channel spine coil. 4D-MRIs were acquired after injection with hepatobiliary contrast (gadoxetic acid) [12] using a T1-weighted 3D fast gradient echo sequence acquired in the axial plane with a golden-angle stack-of-stars sampling trajectory (TE/TR = 1.4/2.8 ms, 1.3 × 1.3 mm voxels, 3 mm slice thickness, FOV = 380 × 380 mm^2, 64–72 slices) [13]. 4D-MRI *k*-space was filled continuously over multiple respiratory cycles (scan time ~8–10 minutes). A self-gating signal (SGS) was extracted from the *k*-space center and used as a respiratory motion surrogate. The Advanced 4D MRI[1] research sequence was used to provide a binning option that separates inhalation and exhalation in the SGS-based motion trace. For consistency with CT, the total number of respiratory bins was chosen as 8. The SGS waveform was first segmented into 4 amplitude bins, and then data in the same bin were separated into inspiration and expiration groups according to the direction of the motion. After respiratory binning, images were reconstructed using a standard radial re-gridding algorithm.

To identify regular and irregular breathers, breathing regularity was quantified using the SGS waveform. The peak-to-trough range and mid-level amplitude (i.e. (peak-amplitude + trough-amplitude) / 2) were calculated for each respiratory cycle. The average mid-level amplitude across all cycles normalized by the average peak-to-trough range was used as the regularity score. Subjects with the score greater than 20% were defined as irregular breathers.

Image analysis

Image quality was assessed using a 4-point Likert scale ('clarity score'). Images were scored as follows:
1   diagnostic quality,
2   non-diagnostic, but clearly demarcated lesion,
3   less clear borders but definable for treatment planning, and
4   lesion undefinable for treatment planning.

Images for each patient were reviewed concurrently by two radiation oncologists and a consensus score was assigned for the end-inspiration and end-expiration phase of each binning technique. Paired *t*-tests were used to compare images and differences were considered statistically significant if p-value < 0.05.

Radiotherapy target delineation and treatment planning

Targets were independently contoured on the 4D-CT and 4D-MRI scans by two radiation oncologists. Gross target volumes (GTV) were contoured on each image phase and internal target volumes (ITV) were generated by summing the GTVs. Planning target volumes (PTVs) were generated by expanding ITVs 8 mm vertically and 5 mm in all other directions. Volumetric information for MR- and CT-derived PTVs were extracted and compared using paired *t*-tests.

4D-CT and 4D-MRI datasets were co-registered by fusing ITVs in the corresponding end-expiration phases. For patients with multiple lesions, separate registrations were performed for each target to account for liver compressibility and rotation. For each patient, a planning CT was generated from the mean intensity projection of the 4D-CT images. All PTVs were transferred to, and OARs were contoured on, this average 4D-CT dataset. To assess dosimetric impacts of MR-derived (PTV$_{MRI}$) and CT-derived (PTV$_{CT}$) targets, radiation plans were optimized separately on each dataset according to the target prescription and OAR objectives used clinically for each patient.

Treatment planning was performed in RayStation (v.7.0 RayStation Laboratories, Stockholm, Sweden) using 10 MV or 10 FFF photon coplanar volumetric modulated arc therapy. Targets were treated to a median dose of 50 Gy in 5 fractions. To maintain consistency and ensure plan quality, all plans were created by a single planner who followed the same workflow that is implemented for clinical patients. To minimize the introduction of biases towards MR- versus CT-optimized plans, each patient's plan was initialized using the same beam orientation and optimization objectives. Thereafter, objectives were adjusted independently during plan optimizations to produce clinically acceptable plans. The proportion of the PTVs receiving 90% of the prescription dose for MR- and CT-derived targets was extracted from the plans optimized for the respective targets. To assess the MR target coverage using CT-optimized plans used in current practice, the PTV coverage for the MR-derived targets was also extracted from the CT-optimized plan. The PTV coverage for MR-derived targets on the MR- and CT-optimized plans were compared to the coverage of CT-derived targets using paired *t*-tests.

Results

Image acquisition

4D-MRIs were obtained for twelve patients with a total of 17 liver tumors. Of the twelve patients, six were classified as regular breathers and six as irregular breathers. Example axial and coronal views of regular and irregular breathers is shown in Figure 1, along with their corresponding respiratory traces and binning results. The binning algorithm was

found to be robust to both regular (Fig. 1A) and irregular (Fig. 1B) breathing patterns.

Image quality was assessed using a 4-point clarity score, with lower clarity scores corresponding to superior image quality, as shown in Figure 2. Clarity scores were significantly better for 4D-MRI versus 4D-CT (1.2 ± 0.4 and 3.5 ± 0.7, respectively, $p < 10^{-9}$). No liver tumors were rated 4 on any 4D-MRI because all lesions were definable on all phases regardless of the binning algorithm. No liver tumors were rated 1 or 2 on any 4D-CT.

Radiotherapy target delineation and treatment planning

On average, there was no significant difference between volumes of MRI-derived and CT-derived targets (39 cc vs. 44 cc, respectively, p = 0.44). Analysis of the radiation plans revealed no significant difference between the dosimetric coverage of 17 CT-derived and MR-derived PTVs on the plans optimized for their respective volumes (PTV receiving 90% of prescription: 89.38% vs. 90.61%, respec-
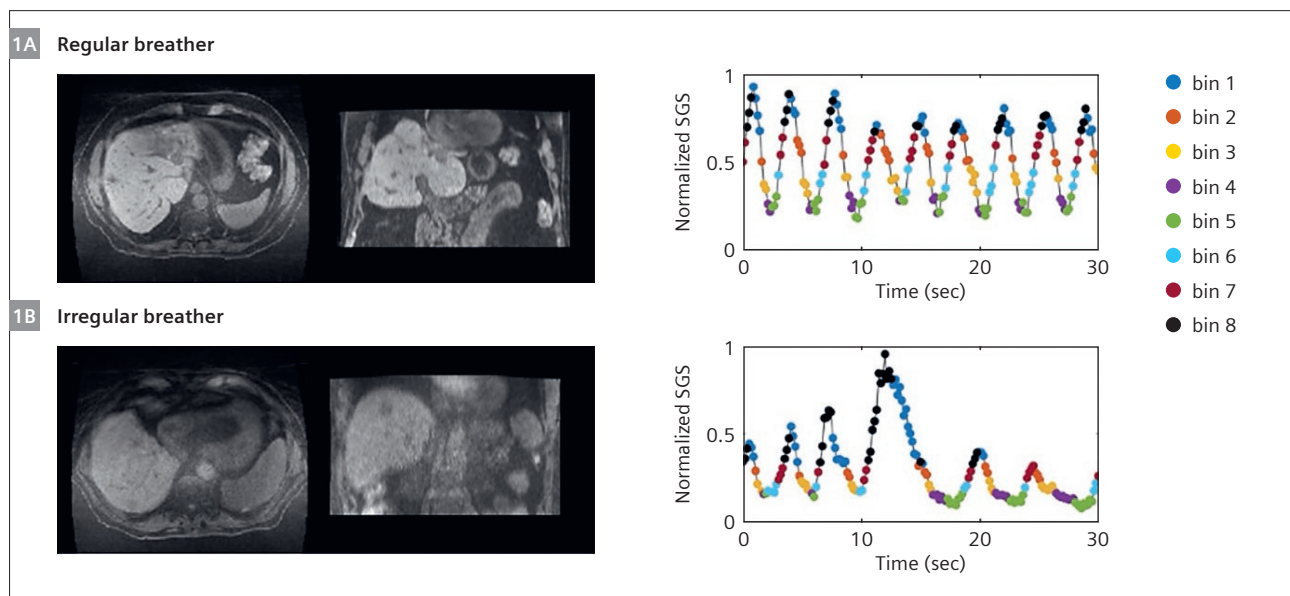
1 Comparison of images and respiratory binning for patients who breathed **(1A)** regularly and **(1B)** irregularly. A 30-second segment of the respiratory self-gating signal (SGS) is also displayed for each binning option. Each point in the waveform has a timing correspondence to a segment of *k*-space data acquisition, and the color represents the bin index assigned to the data.
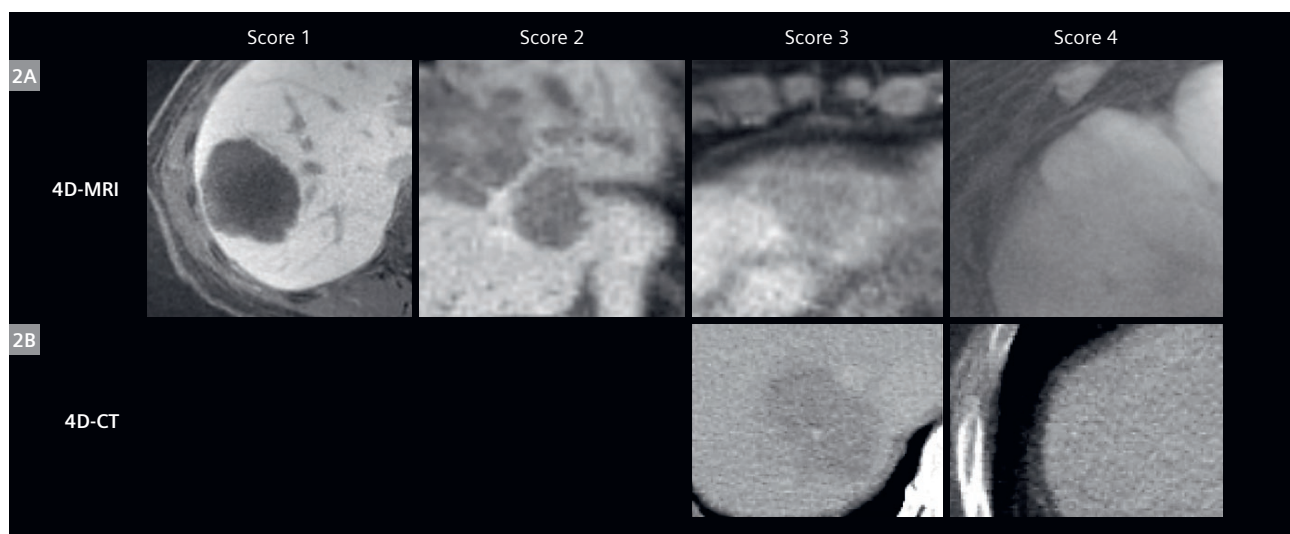
2 Atlas depicting the Likert-4 scale qualitative assessment of image quality of tumors on 4D-MRI **(2A)** and 4D-CT **(2B)** reconstructions. Score legend: (1) diagnostic quality, (2) non-diagnostic, but clearly demarcated lesion, (3) less clear borders but definable for treatment planning, and (4) lesion undefinable for treatment planning. There were no 4D-CT images scored at values of 1 or 2.

tively, p = 0.68) demonstrating similar plan quality for the targets. However, a comparison of the PTV coverage on the CT-optimized plan revealed significantly lower coverage of MR-derived compared to CT-derived targets (PTV receiving 90% of prescription: 75.56% vs. 89.38%, p = 0.002), indicating that planning to the 4D-CT-derived target would result in underdosing of the tumor (Fig. 3). There was no significant difference in the mean liver dose including the PTVs (16.34 Gy vs. 15.2 Gy, respectively, p = 0.29) or the doses to additional organs at risk for CT- and MR-optimized plans (p > 0.05), as OAR sparing had priority over target coverage.

Discussion

Accurately delineating liver tumors is essential for delivering radiation dose to the desired targets while minimizing radiation to normal tissues. In this study, we demonstrate the feasibility of using contrast-enhanced 4D-MRI for the direct visualization of liver tumors throughout the respiratory cycle for ITV generation. Estimating the motion of liver tumors on 4D-CT is fraught with uncertainty because detailed internal anatomy cannot be seen. In contrast, the reliable direct visualization of liver tumors during the respiratory cycle using 4D-MRI facilitates the production of ITVs that accounts for respiratory hysteresis and tissue compressibility.

We adopted a 4D-MRI technique that performs continuous volumetric scanning with self-gating and respiratory binning using a 3D T1-weighted fast gradient echo sequence and a golden-angle radial acquisition scheme. This acquisition scheme is inherently more robust to motion artifacts compared to Cartesian acquisition and allows high-frequency sampling of the center of *k*-space, from which a respiratory motion trace can be derived. As the motion trace is extracted from the acquired data itself, there is no need for external respiratory devices or surrogates. In contrast to 4D-CT acquisition, which acquires data through a single respiratory cycle, this 4D-MRI approach continuously samples breathing over several minutes, with the final average over multiple respiratory cycles potentially being more representative of patients' normal breathing versus helical 4D-CT.

The dosimetric data demonstrated that the use of 4D-MRI may improve radiation targeting of liver tumors. In our study, MRI-generated ITVs tended to be smaller than CT-derived ITVs, although the difference was not statistically significant. Dosimetric data for radiation plans showed similar coverage when optimized for CT-derived and MR-derived targets and dose to adjacent organs at risk, though the significantly lower MR-derived target coverage on CT-optimized plans suggests that the current methods of treatment planning may lead to tumor underdosing and increase the risk of marginal misses. It is unclear how much the difference in ITV generation contributes to the local recurrence of tumors after SBRT, as tumor control is generally high (> 90%) but recurrences could be due to marginal misses resulting from the under-contouring of tumor positions during respiration. Additional research is needed on the clinical impact using MR-based targets on tumor control and tissue toxicity.

Reducing MRI acquisition time is advantageous for many reasons including increased patient comfort and hospital throughput. One method for MRI acceleration is through compressed sensing (CS), however, the effects of CS acceleration on 4D-MRI in the context of radiotherapy treatment planning has not yet been investigated. Our group is investigating the compressed sensing capabilities currently available in the Advanced 4D MRI research sequence. Figure 4 shows example axial and coronal views of a (4A) 4D-CT, (4B) original 4D-MRI (~10-minute acquisition), and simulated 4D-MRI acceleration rate (R) of (4C) R = 2 (~5-minute acquisition), (4D) R = 3 (~3.3-minute acquisition), and (4E) R = 6 (~1.7-minute acquisition).
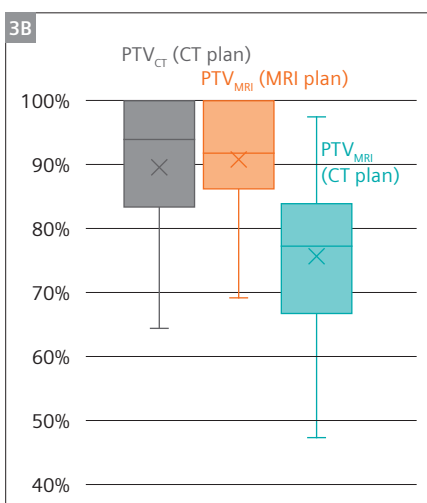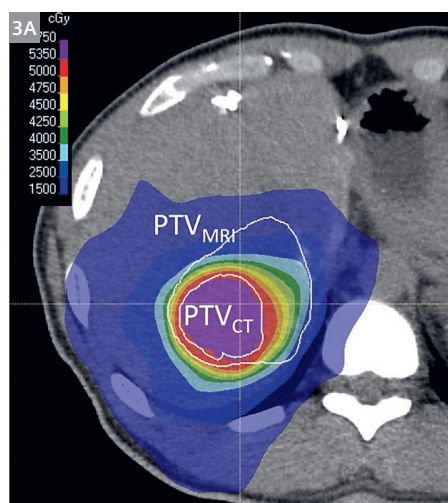
3 (3A) Example axial slice of a radiation treatment plan optimized using CT-derived target volume ('CT plan'). The inner white line shows the CT-derived target (PTV$_{CT}$), the outer white line shows the MR-derived target (PTV$_{MRI}$), and the colored regions correspond to isodose lines. (3B) A boxplot distribution for all 17 PTVs covered by 90% of the prescription dose shows a similar distribution of PTV coverage between CT-derived (gray) and MR-derived (orange) targets on plans optimized for their respective volumes and lower coverage of MRI-derived (petrol) targets for CT-optimized plans.
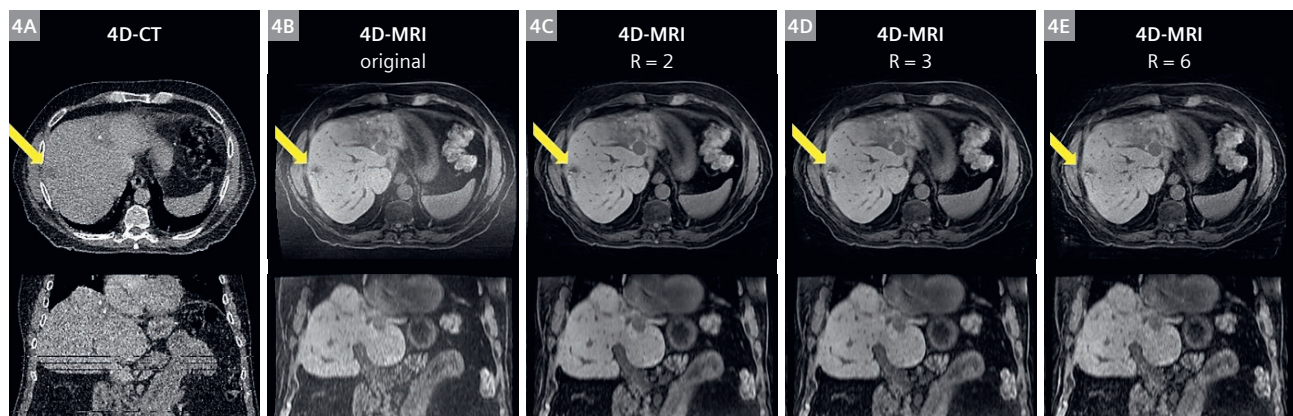
4 Example axial and coronal slices of exhale phase **(4A)** 4D-CT and 4D-MRIs reconstructed using **(4B)** original 3000 spoke sampling and acceleration factors (R) **(4C)** R = 2, **(4D)** R = 3, and **(4E)** R = 6. The liver tumor is annotated using the yellow arrow in all axial planes. Note that the 4D-MRI improves tumor contrast and resolves respiratory-induced motion artifacts relative to the 4D-CT.

Overall, there are many factors that can impact 4D-MRI image quality, including the breathing pattern of the subject, choices of sparsity constraints and regularization weighting in the CS algorithm, and SGS signal processing. The impacts of these factors are currently being investigated using a 4D MRI motion phantom.

Conclusion

This study demonstrates the feasibility of using hepatobiliary contrast-enhanced 4D-MRI to delineate gross liver tumors directly throughout the respiratory cycle. The lower coverage of directly visualized MRI targets in plans generated using standard of care 4D-CT-derived targets suggests that the adoption of 4D-MRI for motion management may improve radiation treatment of liver lesions and reduce the risk of marginal misses. Future investigations will focus on impacts of compressed sensing acceleration and ground-truth measurements in a 4D-MRI phantom.

References

1   Mahadevan A, Blanck O, Lanciano R, et al. Stereotactic Body Radiotherapy (SBRT) for liver metastasis – clinical outcomes from the international multi-institutional RSSearch® Patient Registry. Radiation Oncology. 2018;13(1):1-11.

2   Ohri N, Tomé WA, Romero AM, et al. Local control after stereotactic body radiation therapy for liver tumors. International Journal of Radiation Oncology* Biology* Physics. 2021;110(1):188-195.

3   Doi H, Beppu N, Kitajima K, Kuribayashi K. Stereotactic body radiation therapy for liver tumors: current status and perspectives. Anticancer Research. 2018;38(2):591-599.

4   Wojcieszynski AP, Rosenberg SA, Brower JV, et al. Gadoxetate for direct tumor therapy and tracking with real-time MRI-guided stereotactic body radiation therapy of the liver. Radiother Oncol. Feb 2016;118(2):416-8. doi:10.1016/j.radonc.2015.10.024

5   Leyendecker JR. Gadoxetate disodium for contrast magnetic resonance imaging of the liver. Gastroenterology & Hepatology. 2009;5(10):698.

6   von Siebenthal M, Szekely G, Gamper U, Boesiger P, Lomax A, Cattin P. 4D MR imaging of respiratory organ motion and its variability. Physics in Medicine & Biology. 2007;52(6):1547.

7   Hu Y, Caruthers SD, Low DA, Parikh PJ, Mutic S. Respiratory amplitude guided 4-dimensional magnetic resonance imaging. International Journal of Radiation Oncology* Biology* Physics. 2013;86(1):198-204.

8   Tryggestad E, Flammang A, Han-Oh S, et al. Respiration-based sorting of dynamic MRI to derive representative 4D-MRI for radiotherapy planning. Medical physics. 2013;40(5):051909.

9   Deng Z, Pang J, Yang W, et al. Four-dimensional MRI using three-dimensional radial sampling with respiratory self-gating to characterize temporal phase-resolved respiratory motion in the abdomen. Magnetic resonance in medicine. 2016;75(4):1574-1585.

10 Van de Lindt TN, Fast MF, van der Heide UA, Sonke J-J. Retrospective self-sorted 4D-MRI for the liver. Radiotherapy and Oncology. 2018;127(3):474-480.

11 Thomas HR, Miao X, Ferguson D, et al. Contrast-enhanced 4D-MRI for internal target volume generation in treatment planning for liver tumors. Radiotherapy and Oncology. 2022;

12 Van Beers BE, Pastor CM, Hussain HK. Primovist, Eovist: what to expect? Journal of hepatology. 2012;57(2):421-429.

13 Grimm R, Block K, Hutter J, et al. Self-gating reconstructions of motion and perfusion for free-breathing T1-weighted DCEMRI of the thorax using 3D stack-of-stars GRE imaging. 2012:3814.

Contact

Jessica Scholey, Ph.D., DABR
Assistant Professor
Director of MRI Simulation
Department of Radiation Oncology
University of California San Francisco
505 Parnassus Ave., Room L-75
San Francisco, CA 94143-0226
USA
Tel.: +1 (415) 353-7191
jessica.scholey@ucsf.edu